Engineering Fracture Mechanics 282 (2023) 109201

Contents lists available at ScienceDirect

Engineering Fracture Mechanics

journal homepage: www.elsevier.com/locate/engfracmech

Debonding model for nonlinear Fe-SMA strips bonded with nonlinear adhesives

Lingzhen Li [a,b,*], Eleni Chatzi [b], Elyas Ghafoori [a,c]

[a] Empa, Swiss Federal Laboratories for Materials Science and Technology, Structural Engineering Research Laboratory, 8600, Dübendorf, Switzerland

[b] Institute of Structural Engineering (IBK), ETH Zürich, 8093, Zürich, Switzerland

[c] Institute for Steel Construction, Faculty of Civil Engineering and Geodetic Science, Leibniz University Hannover, 30167, Hannover, Germany

ARTICLE INFO

Keywords:
Memory steel
Iron-based shape memory alloys (Fe-SMAs)
Bond capacity
Interfacial fracture energy
Bond–slip behavior
Full-range behavior

ABSTRACT

The application of adhesively-bonded joints for strengthening of structures using iron-based shape memory alloys (Fe-SMAs) has recently emerged in construction. Fe-SMAs and the majority of structural adhesives exhibit a pronounced nonlinear material behavior, which may result in a favorable ductile failure mechanism. The development, however, of a mechanical model to predict the structural behavior of the joint is non-trivial due to the presence of nonlinearity in the adherent and adhesive. This study aims to propose a semi-analytical and semi-numerical model for describing the mechanical behavior of Fe-SMA-to-steel adhesively bonded joints. The developed model serves three main functions: (i) estimating the bond capacity for a given interfacial fracture energy, and vice versa; (ii) processing the bond–slip ($\tau - s$) behavior directly from the load–displacement ($F - \Delta$) curve, and vice versa; and (iii) delivering a numerical method to simulate the full-range mechanical behavior of the bonded joints, namely the behavior at different loading stages. The model is validated using the experimental testing of 26 Fe-SMA-to-steel lap-shear joints, as well as 24 further bonded joints subject to shear with different adherents (e.g., stainless steel strips and Nickel–Titanium SMA wires) and base materials (e.g., concrete and composite polymer). An experimental data processing protocol, on the basis of the experimentally measured force–displacement ($F - \Delta$) behavior and the distributed displacement along the bond line ($s - x$) via the Digital Image Correlation (DIC) technique, is further proposed to assess the full-range behavior of bonded joints.

1. Introduction

Iron-based Shape Memory Alloys (Fe-SMAs) have shown great potential for rehabilitation of steel structures [1–4], thanks to the stability of prestress and ease of application, the recoverable prestress loss via the process of re-activation [5,6], the satisfactory mechanical properties (elastic modulus), and the relatively low price (a slight multiple of the price of mild steel). The prestress, which is beneficial for enhancing the mechanical performance of steel structures, can be easily effectuated by heating the prestrained Fe-SMA strip followed by a cooling process, due to a martensite to austenite phase transformation [7]; this process is known as the activation of prestress. The generated prestress is transferred to the parent structure via (i) mechanical anchorages, including mechanical fixtures [1,2] and nail anchorages [3], or (ii) adhesively bonded anchorages [4,8,9]. Such a strengthening strategy,

* Corresponding author at: Empa, Swiss Federal Laboratories for Materials Science and Technology, Structural Engineering Research Laboratory, 8600, Dübendorf, Switzerland.

E-mail addresses: lingzhen.li@empa.ch (L. Li), chatzi@ibk.baug.ethz.ch (E. Chatzi), ghafoori@stahl.uni-hannover.de (E. Ghafoori).

https://doi.org/10.1016/j.engfracmech.2023.109201
Received 22 September 2022; Received in revised form 25 January 2023; Accepted 13 March 2023
Available online 15 March 2023

Nomenclature

Δ	Displacement at the loaded end
$\sigma - x$	Tensile stress profile of adherent
σ	Tensile stress of the adherent
$\tau - s$	Bond–slip behavior
$\tau - x$	Shear stress profile along the bond line
τ	Shear stress in the bond line
τ_i	Shear stress at point-i
$\varepsilon - x$	Tensile strain profile of adherent
ε	Tensile strain of the adherent
ε_i	Tensile strain of the adherent at point-i
b	Bond width
E	E-modulus of the adherent
E_{SMA}	Elastic modulus of the Fe-SMA
$F - \Delta$	Force–displacement behavior
F	Tensile force at the loaded end
F_b	Bond capacity
F_i	Tensile force carried by the adherent at point-i
G_f	Fracture energy of the adhesive bond
$G_{f,i}$	Partial fracture energy
s	Slip
s_i	Slip at point-i
s_u	Maximum slip in the bond–slip behavior
t	Thickness of the adherent
U_{SMA}	Displacement of the Fe-SMA strip in the loading direction
U_{steel}	Displacement of the steel plate in the loading direction
x	Coordinate in the loading direction
x_i	Coordinate at point-i
CFRP	Carbon fiber reinforced polymer
CZM	Cohesive zone model
dσ	Tensile stress increment
dε	Tensile strain increment
DIC	Digital image correlation
Fe-SMA	Iron-based shape memory alloy
LDT	Laser displacement transducer
LVDT	Linear variable differential transformer
NiTi-SMA	Nickel–Titanium shape memory alloy

adopting mechanical anchoraging, has been implemented in laboratory conditions [1,3] and successfully applied to enhance the load bearing capacity and fatigue performance of a roadway bridge constructed in 1906 in Petrov nad Desnou (Czech Republic) [2]. However, when the use of mechanical anchorages is restricted, for instance, when drilling holes to the parent structure is not favored, the bonded strengthening solution provides further benefits, such as (i) no damage to the parent structure, (ii) gradual stress transfer along the bond line, and (iii) additional local stiffening for cracked steel elements [10].

A concept of partial activation of prestress was proposed by Wang et al. [4]. A prestrained Fe-SMA strip is bonded to the target location of a steel member (see Fig. 1). The prestress is activated by heating the middle section of the Fe-SMA strip followed by a cooling process, while the two ends remain unheated and serve as the bonded anchorages, which transfer the prestress to the parent structure. In order to apply such a bonded strengthening technique effectively, it is crucial to understand the mechanical behavior of Fe-SMA-to-steel interfaces. However, very few studies have been conducted in this respect. The experimental studies delivered by Wang et al. [8] and Li et al. [9] suggest that a nonlinear (also known as ductile) adhesive offers higher fracture energy, greater bond capacity, and larger ductility to a bonded joint with respect to application of a linear (also known as brittle) adhesive. Under adoption of a nonlinear adhesive as the bonding agent, the stress–strain behavior of Fe-SMA strip enters the nonlinear stage.

The investigation of the behavior on similar bonded joints can enhance our understanding of Fe-SMA-to-steel joints. In the past two decades, the CFRP-to-concrete and CFRP-to-steel bonded joints have been intensively investigated via experimentation [11–14] and modelling [15–18]. The analysis is, however, mostly conducted on the assumption of a linear CFRP material. For instance, the

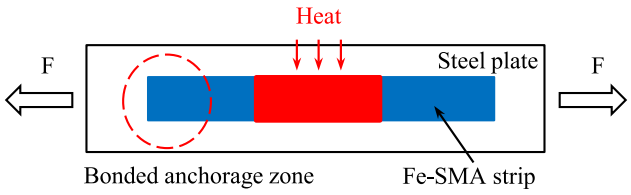

Fig. 1. Schematic view of a steel plate strengthened by means of a bonded Fe-SMA strip.

well-established model, per Eq. (1), which estimates the load transferring capacity (bond capacity) of CFRP bonded joints [11,13,16,17,19,20], relies exclusively on the assumption of a constant E-modulus and the geometric characteristics. Furthermore, analytical solutions of the full-range behavior, namely the behavior at different loading stages, of CFRP bonded joints are derived on the basis of the same assumption [15,18,21].

$$F_b = b \cdot \sqrt{2 \cdot E \cdot t \cdot G_f} \tag{1}$$

where F_b denotes the bond capacity; b and t are the bond width and CFRP thickness, respectively; E represents the elastic modulus of CFRP; G_f reflects the interfacial fracture energy of the adhesive layer (CFRP-to-steel bond) or of the concrete (CFRP-to-concrete bond).

When an Fe-SMA strip is bonded by a linear adhesive, the fracture energy of the bond line is low, and the stress–strain of Fe-SMA remains in its quasi-linear stage [9]. In this case, the Fe-SMA can be simplified as a linear-elastic material and characterized by its secant modulus; models for CFRP bond including Eq. (1) still perform well in such a case. On the other hand, when a nonlinear adhesive is employed, the Fe-SMA experiences nonlinear stress–strain behavior [8,9]. In this case, the existing knowledge built on CFRP bonded systems cannot be applied directly to the Fe-SMA-to-steel bond, thus necessitating an appropriate nonlinear model, which can be used for design purposes.

Recently, Silvestru et al. [22] and Deng et al. [23] conducted experimental and numerical studies, respectively, to investigate the behavior of Fe-SMA-to-glass bonded joints which employ nonlinear adhesives. The failure observed in the examined joints [22] is a mixture of (i) damage inside the continuous adhesive layer (cohesion failure), (ii) detachment in the adhesive-glass interface (adhesion failure), and (iii) fracture of glass panels, whereas that in Fe-SMA-to-steel bonded joints is predominantly cohesion failure [9]. On the other hand, the focus of finite element models conducted by Deng et al. [23] lies in the influence of the geometry of a joint on the load–displacement behavior.

In addition, an important feature of Fe-SMA-to-steel bonded joints is the effective bond length, beyond which the bond capacity does not further increase [8,9]. Such a trait was also observed in Fe-SMA-to-glass bonded joints [22,23]. The effective bond length does not exist in joints with internal reinforcing bars or wires, such as Nickel–Titanium Shape Memory Alloy (NiTi-SMA) rebars embedded in concrete [24–26], NiTi-SMA wires embedded in composites [27–29], and Fe-SMA rebars embedded in concrete [30–32]. In these cases, the tensile strength of SMA rebars and wires can be achieved with a sufficient anchorage length. Numerical simulations based on Cohesive Zone Modeling (CZM) were developed in such cases for inferring the interfacial bond–slip behavior and for simulating the full-range behavior [27,28,31]. However, to the knowledge of the authors, no analytical solution is available for predicting the bond capacity, or for inferring the interfacial response for joints comprising both nonlinear adherents and adhesives.

This study aims to fill the existing knowledge gap by proposing a simplified one-dimensional lap-shear model, which is semi-analytical and semi-numerical in nature, to simulate the mechanical response of Fe-SMA-to-steel bonded joints subject to quasi-static loading. In Section 3, an analytical model with two functions is proposed: (i) a reversible nonlinear relationship between the bond capacity and the interfacial fracture energy, based on the stress–strain relationship of the Fe-SMA; (ii) a nonlinear relationship delivering an invertible mapping of the global load–displacement behavior to the local bond–slip behavior. In Section 4, a numerical model, which admits the Fe-SMA stress–strain relationship and bond–slip characteristics as input, is proposed to simulate the full-range lap-shear behavior, including the tensile stress and strain of the Fe-SMA strip, the shear stress distribution along the bond line at different loading stages, and the load–displacement behavior. In Section 5, an experimental data processing method, based on the measured slip along the bond line ($s - x$) and the force–displacement ($F - \Delta$) behavior, is proposed for inferring the behavior of bonded joints; the inferred experimental behavior of 24 lap-shear specimens from a parallel study [9] and two more tested very recently by the authors are used to validate the proposed numerical model. It is observed that the mechanical behavior of the bonded joints is closely approximated by the proposed model. In the last part (Section 6), 24 more bonded joints subject to shear load (e.g., Fe-SMA rebars embedded in concrete blocks and NiTi-SMA wires embedded in composite polymers) are collected from the literature and used to further validate the proposed model, whose applicability is proven valid beyond the specific case of Fe-SMA-to-steel bonded joints.

2. Experimental campaign

26 lap-shear tests on Fe-SMA-to-steel bonded joints were conducted by the authors, among which 24 were reported in an experimental study [9]. The further two were tested recently, with details summarized in Appendix A. A short summary of the

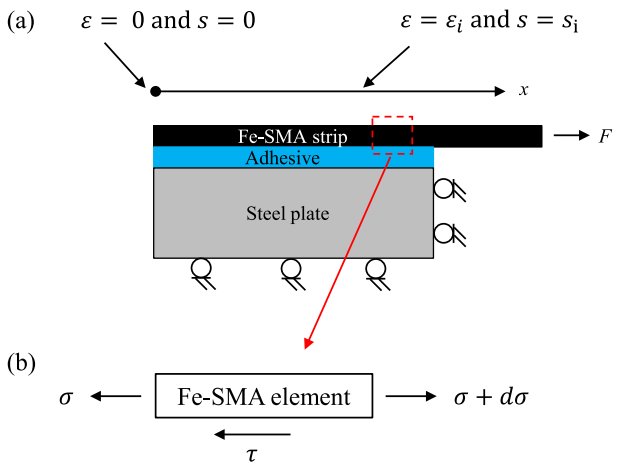

Fig. 2. (a) Schematic plot of the lap-shear model, with boundary conditions specified as $\epsilon|_{x=0} = 0$ and $s|_{x=0} = 0$, while $\epsilon|_{x=x_i} = \epsilon_i$ and $s|_{x=x_i} = s_i$. (b) Equilibrium of an Fe-SMA infinitesimal element in the loading direction, with σ and τ representing tensile stress in the cross-section and shear stress at the strip bottom, respectively.

primary test parameters is offered herein. The test campaign comprises two types of Fe-SMA strips (non-prestrained and prestrained), four types of adhesives (one linear adhesive and three nonlinear adhesives), and three thickness values for the adhesive layer (0.5, 1, and 2 mm). Fig. 2a depicts a schematic plot of the lap-shear specimen, in which the Fe-SMA strip comprises a length of 600 mm, a width of 50 mm, and a thickness of 1.5 mm, while the bond length is 300 mm. All specimens were tested under a displacement-controlled loading regime with a loading speed of 0.02 mm/s until failure, i.e., full debonding or rupture of the Fe-SMA strip. During the tests, a load cell of 150 kN capacity was used to measure the tensile force. The Digital Image Correlation (DIC) technique was used to measure a full-field displacement and strain, which were further used to infer the shear behavior. For further details, the interested reader is referred to the experimental study [9]. The test results are used for validation of the model proposed in the following sections.

3. Nonlinear bonded joint modelling

In the following sections, a semi-analytical and semi-numerical model is proposed. It serves three main functions: (i) to offer a nonlinear mapping between the fracture energy of the adhesive bond and the bond capacity of the joint, (ii) to allow for processing of the local bond–slip ($\tau - s$) behavior directly from the global load–displacement ($F - \Delta$) curve, and vice versa, and (iii) to deliver a numerical scheme to simulate the full-range mechanical behavior of bonded joints.

3.1. Model setup

In this study, the shear behavior of the adhesive bond is described as a bond–slip behavior (shear stress vs. shear deformation). The shear deformation, also known as slip (s, relative displacement between the Fe-SMA strip and the steel plate), is expressed as Eq. (2). Since the steel plate is much stiffer than the Fe-SMA strip, its deformation can be neglected, allowing the engineering tensile strain (referred to as tensile strain hereinafter) of the Fe-SMA strip to be expressed as in Eq. (3).

$$s = U_{SMA} - U_{steel} \tag{2}$$

$$\epsilon = \frac{\mathrm{d}U_{SMA}}{\mathrm{d}x} = \frac{\mathrm{d}s}{\mathrm{d}x} + \frac{\mathrm{d}U_{steel}}{\mathrm{d}x} \approx \frac{\mathrm{d}s}{\mathrm{d}x} \tag{3}$$

where U_{SMA} and U_{steel} represent the displacement of the Fe-SMA strip and the steel plate, respectively; s and ϵ denote the slip and tensile strain of the Fe-SMA strip, respectively; and x denotes the coordinate in the loading direction.

By isolating an infinitesimal element of the Fe-SMA strip depicted in Fig. 2b, the equilibrium is written per Eq. (4).

$$\frac{\mathrm{d}\sigma}{\mathrm{d}x} = \frac{\tau}{t} \Longrightarrow \frac{\mathrm{d}\sigma}{\mathrm{d}\epsilon}\frac{\mathrm{d}\epsilon}{\mathrm{d}x} = \frac{\tau}{t} \tag{4}$$

where σ and τ represent tensile and shear stress, respectively; t denotes the thickness of the Fe-SMA strip.

The combination of Eqs. (3) and (4) yields Eq. (5) [13].

$$\epsilon\frac{\mathrm{d}\sigma}{\mathrm{d}\epsilon}\frac{\mathrm{d}\epsilon}{\mathrm{d}x} = \frac{\tau}{t}\frac{\mathrm{d}s}{\mathrm{d}x} \tag{5}$$

If the length of the adhesive bond is sufficiently long (no shorter than the effective bond length), the free end ($x = 0$, the left end in Fig. 2a) is unloaded, and the boundary conditions at $x = 0$ are expressed as Eq. (6). The bond length in the current study

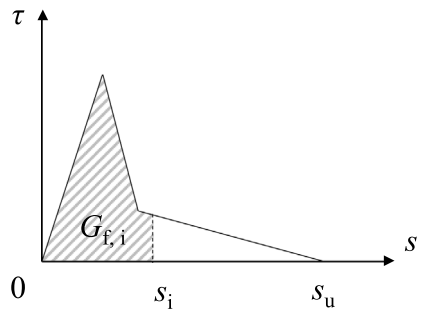

Fig. 3. Schematic bond–slip curve and the partial fracture energy, with s_u denoting the maximum slip and s_i being the slip of point-i. The area covered by the bond–slip curve is the fracture energy (G_f), while the area truncated by s_i is the partial fracture energy ($G_{f,i}$).

is assumed as 300 mm, identical to the bond length in the experimental campaign (Section 2). Wang et al. [8] and Li et al. [9] determined the effective bond length of Fe-SMA-to-steel bonded joints being approximately 70–160 mm, via analyzing the shear stress profile ($\tau - x$) processed from the experimentally measured behavior. Since the assumed bond length exceeds the effective bond length, the boundary conditions specified in Eq. (6) hold. The strain and slip at a random position x_i along the bond line are offered by Eq. (7).

$$\varepsilon(0) = 0, s(0) = 0 \tag{6}$$

$$\varepsilon(x_i) = \varepsilon_i, s(x_i) = s_i \tag{7}$$

The integral of Eq. (5) with respect to coordinate (x) from the free end to point-i along the bond line, i.e., over the interval (0, x_i), yields:

$$\int_0^{x_i} \varepsilon \frac{\mathrm{d}\sigma}{\mathrm{d}\varepsilon}\frac{\mathrm{d}\varepsilon}{\mathrm{d}x}\mathrm{d}x = \int_0^{x_i} \frac{\tau}{t}\frac{\mathrm{d}s}{\mathrm{d}x}\mathrm{d}x \Longrightarrow \int_0^{\varepsilon_i} \varepsilon \frac{\mathrm{d}\sigma}{\mathrm{d}\varepsilon}\mathrm{d}\varepsilon = \int_0^{s_i} \frac{\tau}{t}\mathrm{d}s \tag{8}$$

Here, a concept of partial fracture energy (or partial interfacial fracture energy) is introduced, which is illustrated in Fig. 3. The interfacial fracture energy (G_f) describes the energy needed to create new unit surfaces in the bond line and reflects the area covered by the bond–slip curve. The partial interfacial fracture energy ($G_{f,i}$), on the other hand, is the energy dissipated at point-i along the bond line and is denoted as the shadowed area in Fig. 3, which can be computed via Eq. (9).

$$G_{f,i} = \int_0^{s_i} \tau \mathrm{d}s \tag{9}$$

where s_i and $G_{f,i}$ are the slip and partial fracture energy at a random position x_i, while τ denotes the shear stress.

$G_{f,i}$ corresponds to the interfacial fracture energy (G_f), when the slip (s_i) equals the maximum slip (s_u), but only forms part of the (total) interfacial fracture energy when the slip (s_i) is lower than the maximum slip (s_u). It has been experimentally observed [8,9] that the shape and area of the bond–slip ($\tau - s$) curves at different locations along a bonded joint prove alike. Motivated by this observation, we here adopt the assumption of invariant bond–slip ($\tau - s$) behavior at different locations along the bond line.

Substituting Eq. (9) into Eq. (8) yields Eq. (10), which links the tensile strain of the Fe-SMA strip to the energy dissipated in the adhesive bond (the partial fracture energy) via a relationship. This is in line with the assumption that the τ–s is location-independent.

$$G_{f,i} = t \cdot \int_0^{\varepsilon_i} \varepsilon \frac{\mathrm{d}\sigma}{\mathrm{d}\varepsilon}\mathrm{d}\varepsilon \tag{10}$$

where $d\sigma/d\varepsilon$ represents the tangential modulus of the Fe-SMA. Once the stress–strain behavior of the Fe-SMA is known, the relationship between the partial fracture energy and the Fe-SMA tensile strain can be expressed explicitly. Based on the observed experimental stress–strain curve of Fe-SMA, a two-term exponential expression of the stress–strain is proposed in this study, as written per Eq. (11); $d\sigma/d\varepsilon$ reads as Eq. (12).

$$\sigma = a_1 \cdot e^{b_1 \cdot \varepsilon} + a_2 \cdot e^{b_2 \cdot \varepsilon} - a_1 - a_2 \tag{11}$$

$$\frac{\mathrm{d}\sigma}{\mathrm{d}\varepsilon} = a_1 \cdot b_1 \cdot e^{b_1 \cdot \varepsilon} + a_2 \cdot b_2 \cdot e^{b_2 \cdot \varepsilon} \tag{12}$$

where σ and ε are the tensile stress and strain of the Fe-SMA, while a_1, a_2, b_1, and b_2 are coefficients to be fitted.

Two types of Fe-SMA, namely non-prestrained and prestrained Fe-SMA, are used in this study. The experimentally measured stress–strain data can be fitted with the analytical form proposed in Eq. (11), with the finally derived coefficients listed in Table 1. The stress–strain curves are plotted in Fig. 4, with very good fit observed between experimental measurements and modelling. It should be stressed, however, that these coefficients do not have a clear physical connotation.

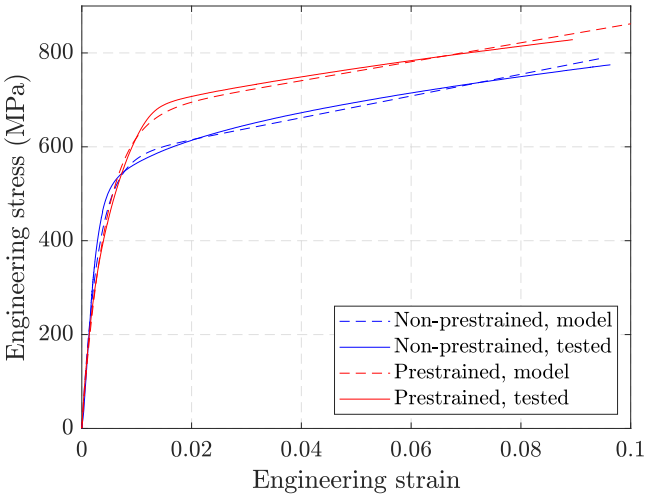

Fig. 4. $\sigma-\varepsilon$ of Fe-SMAs. The experimentally measured $\sigma-\varepsilon$ (solid curves) and the two-term exponential $\sigma-\varepsilon$ model (dashed curves). Blue curves represent the non-prestrained Fe-SMA, while the red curves represent the prestrained Fe-SMA.

Table 1
Coefficients in the $\sigma-\varepsilon$ model of the two Fe-SMAs.

	a_1	b_1	a_2	b_2
Non-prestrained SMA	1.777e05	0.01303	−569.3	−342.8
Prestrained SMA	7.323e04	0.02753	−660.2	−239.1

Further substitution of Eq. (12) into Eq. (10) yields Eq. (13), which has a twofold significance. Firstly, once the tensile strain of the Fe-SMA strip at any point is known, the corresponding energy dissipation of the adhesive bond can be computed (this will lead to Section 3.2). Secondly, on the basis of Eq. (13), the local bond–slip ($\tau-s$) relationship can be processed directly from the global load–displacement ($F-\Delta$) behavior (this will lead to Section 3.3). Eq. (13) is further noted as Eq. (14) for the sake of simplification.

$$G_{f,i}=t\cdot\left[\frac{a_1\cdot e^{b_1\cdot\varepsilon_i}\cdot(b_1\cdot\varepsilon_i-1)}{b_1}+\frac{a_2\cdot e^{b_2\cdot\varepsilon_i}\cdot(b_2\cdot\varepsilon_i-1)}{b_2}+\frac{a_1}{b_1}+\frac{a_2}{b_2}\right] \tag{13}$$

$$G_{f,i}=f_1(\varepsilon_i) \tag{14}$$

where $G_{f,i}$ and ε_i represent the partial fracture energy and Fe-SMA tensile strain, respectively, at a random position x_i; t denotes the thickness of the Fe-SMA strip; a_1, a_2, b_1, and b_2 are fitted coefficients.

3.2. Prediction of the bond capacity with given G_f

Along the bond line, the tensile force carried by the Fe-SMA strip is expressed as in Eq. (15). Substituting the inversed Eq. (14) into Eq. (15) yields Eq. (16), which directly links, at a random position x_i, the dissipated energy (partial interfacial fracture energy, $G_{f,i}$) to the internal tensile force carried by the Fe-SMA strip.

$$F_i=\sigma_i\cdot A=f_2(\varepsilon_i) \tag{15}$$

$$F_i=f_2(f_1^{-1}(G_{f,i})) \tag{16}$$

where the subscript i denotes a random position x_i; F_i, σ_i, and ε_i are the internal tensile force, tensile stress, and tensile strain of the Fe-SMA strip; A represents the cross-sectional area of the Fe-SMA strip; $G_{f,i}$ reflects the partial fracture energy.

When debonding initiates, the adhesive bond at the loaded end is fully damaged, thus, $G_{f,i}$ becomes the interfacial fracture energy G_f, and F_i represents the bond capacity. Correspondingly, Eq. (16) is used to compute the bond capacity of the Fe-SMA-to-steel adhesively bonded lap-shear joint at a given interfacial fracture energy. A perfect match between the model prediction (curves) and the experimental observation (dots) is illustrated in Fig. 5, where the fracture energy is computed as the area covered by the experimental processed bond–slip curve [9]. Fig. 5 further reveals that an interfacial fracture energy value of ca. 2.6 MPa·mm leads to the same bond capacity (ca. 44.5 kN) for joints with both the prestrained non-prestrained Fe-SMAs. This interfacial fracture energy value, G_f = 2.6 MPa·mm, is used to classify the adhesives used in this study as linear, when they correspond to a lower G_f and nonlinear for higher G_f values. The following conclusion, on the basis of observation of Fig. 5, which is in line with the experimental

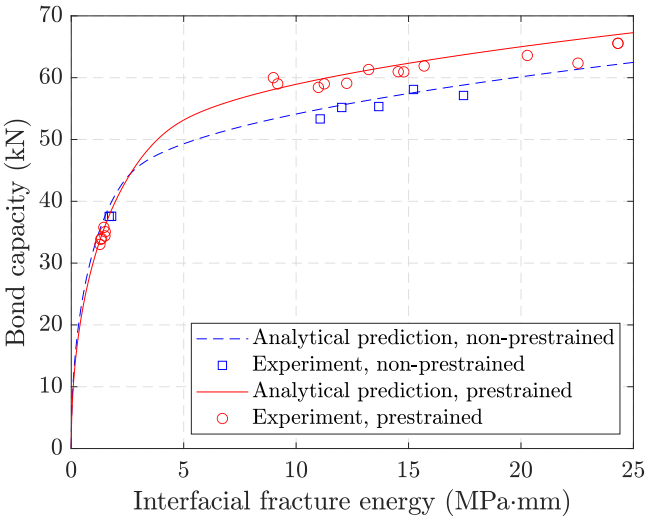

Fig. 5. Bond capacity vs. interfacial fracture energy. The dashed blue and solid red curves reflect the model prediction (Eq. (16)) for non-prestrained (– – –) and prestrained (—) Fe-SMAs, respectively. Blue squares and red circles correspond to experimental data for non-prestrained (□) and prestrained (○) Fe-SMAs, respectively. In the tests, bond capacity is defined as the maximum force recorded by the load cell. The interfacial fracture energy corresponds to the area under the experimentally derived bond–slip curves [9].

observation in Li et al. [9], can then be drawn: when a linear adhesive is utilized for bonding, a joint with a non-prestrained Fe-SMA strip possesses slightly higher bond capacity; when bonded joints utilize a nonlinear adhesive, a joint with a prestrained Fe-SMA possesses higher bond capacity.

Eq. (16) can further be converted to Eq. (17), which estimates the fracture energy of the adhesive bond with an experimentally measured bond capacity.

$$G_{f,i} = f_1(f_2^{-1}(F_i)) \tag{17}$$

where $G_{f,i}$ and F_i are the partial fracture energy and Fe-SMA internal tensile force, respectively, at position-i; when computed at the loaded end, these correspond to the fracture energy and bond capacity, respectively.

3.3. Inferring bond–slip behavior from load–displacement curve

Once the fracture energy is obtained, the next step is to infer the bond–slip behavior, which will later be used in the modelling of the full-range behavior of bonded joints. A commonly adopted approach (referred to as the traditional method hereinafter) [8,9,22] to infer the bond–slip relationship is described as follows: (i) the tensile strain of the Fe-SMA strip is experimentally derived (e.g. via use of the DIC technique); (ii) the tensile stress is computed on the basis of the stress–strain relationship; (iii) the shear stress is derived on the basis of the equilibrium of the Fe-SMA infinitesimal elements, as demonstrated in Fig. 2b. Such a method has been widely adopted in studies of CFRP bonded joint [11,13,33–37]. In this work, we propose a new approach to derive the local bond–slip ($\tau - s$) directly from the global load–displacement ($F - \Delta$), without the requirement for a strain reading, which cannot be easily made available outside a laboratory setting.

Focusing on the loaded end of the bonded joint (the right end in Fig. 2a), the force is read by the load cell during the experimental procedure, while the displacement is read via use of DIC on images obtained with an appropriate high resolution camera. As aforementioned, by ignoring the deformation of the steel plate, the Fe-SMA displacement at the loaded end of the bond can be regarded as the slip at that location. Therefore, the measured load–displacement ($F - \Delta$) curve can be denoted as in Eq. (18). Substituting Eq. (18) into Eq. (17) yields Eq. (19), which describes the relationship between the partial fracture energy ($G_{f,i}$) and the simultaneous slip, namely correlating the shadow area and the slip (s_i) in Fig. 3. The derivative of Eq. (9) with respect to slip (s) yields Eq. (20). Further substitution of Eq. (19) into Eq. (20) yields Eq. (21), which delivers the bond–slip ($\tau - s$) behavior.

$$F_i = f_3(s_i) \tag{18}$$

$$G_{f,i} = f_1(f_2^{-1}(f_3(s_i))) \tag{19}$$

$$\tau_i = \frac{\mathrm{d}G_{f,i}}{\mathrm{d}s} \tag{20}$$

$$\tau_i = \frac{\mathrm{d}f_1(f_2^{-1}(f_3(s_i)))}{\mathrm{d}s} \tag{21}$$

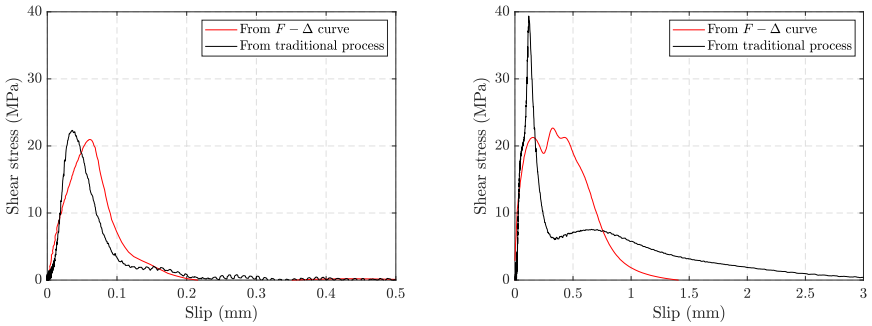

(a) Joint with linear adhesive (b) Joint with nonlinear adhesive

Fig. 6. Comparison of the bond–slip behavior ($\tau - s$) inferred from experimentally measured load–displacement curves (in red, —) and those processed by a traditional method [9] (in black, —).

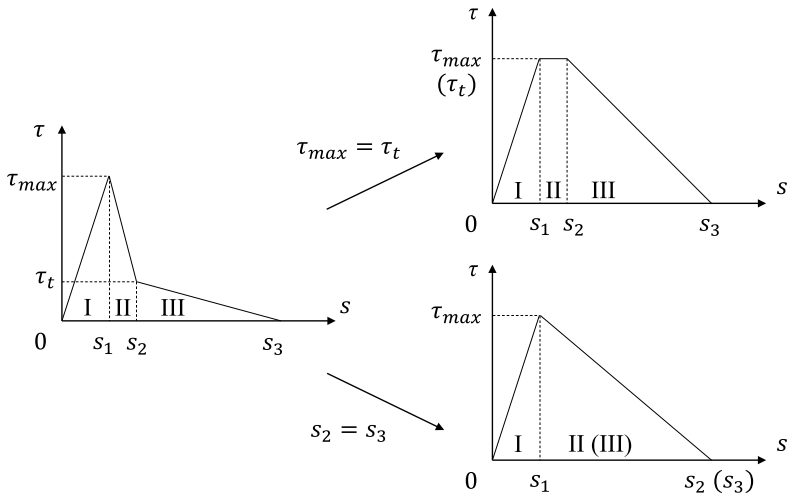

Fig. 7. The trilinear bond–slip model and its variants: trapezoidal model with $\tau_t = \tau_{max}$ and triangular model with $s_2 = s_3$.

where the subscript i represents a random position x_i along the bond line; F_i denotes the internal tensile force carried by the Fe-SMA strip; τ_i, s_i, and $G_{f,i}$ are the shear stress, slip, and partial fracture energy, respectively, in the bond line.

Fig. 6 shows two examples of the bond–slip ($\tau - s$) behavior processed from the load–displacement curves (in red, —), with the black (—) being processed using the traditional method. A comparison of the obtained bond–slip ($\tau - s$) curves for different schemes indicates that the proposed method closely approximates the traditional approach when processing joints with a linear adhesive, since both bond–slip curves (red and black) reflect a similar (triangular) shape and area. However, when processing joints with a nonlinear adhesive, the current method corresponds to a bond–slip behavior which can be simplified to a trapezoidal shape, as shown in Fig. 6(b) in red (—), while the traditional method results in a trilinear bond–slip, as shown in Fig. 6(b) in black (—). This differentiation is owed to the two dimensional nature of the stress state along the bond line, which though lies outside the scope of this paper, and will not be elaborated upon. Hereinafter, the bond–slip behavior is processed by the current model (i.e., Eqs. (18) to (21)).

3.4. Simulating load–displacement curve based on triangular and trapezoidal bond–slip behavior

Similarly, the load–displacement ($F - \Delta$) behavior can be easily computed with a given bond–slip ($\tau - s$) behavior. As illustrated in Section 3.3, different shapes have been observed for bond–slip ($\tau - s$), including a triangular bond–slip ($\tau - s$) for linear adhesives and a trilinear or trapezoidal bond–slip ($\tau - s$) for nonlinear adhesives. Here, we introduce a bond–slip ($\tau - s$) model with three stages (trilinear $\tau - s$ model), which is depicted in Fig. 7 and mathematically described as Eq. (22). The trilinear model corresponds to a trapezoidal model, when $\tau_{max} = \tau_t$, and degenerates into a bilinear (triangular) model, when s_2 and s_3 collapse.

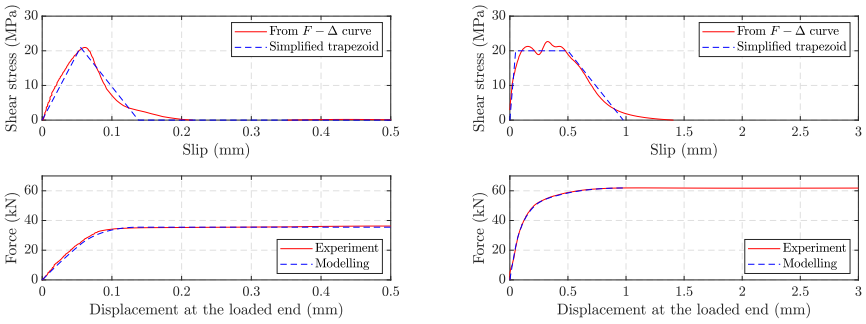

(a) Joint with linear adhesive (b) Joint with nonlinear adhesive

Fig. 8. Load–displacement ($F-\Delta$) computed from the simplified bond–slip ($\tau-s$) curves. The red bond–slip curves are processed from load–displacement via Eqs. (18) to (21), while the blue dashed bond–slip curves are simplification of red ones. The red load–displacement curves are measured during the tests, while the blue load–displacement are simulated via Eq. (25).

$$\tau_i = \begin{cases} \frac{\tau_{max}}{s_1}\cdot s_i, & 0 \le s_i \le s_1 \\ \frac{\tau_{max}-\tau_t}{s_1-s_2}\cdot s_i + \frac{\tau_t\cdot s_1-\tau_{max}\cdot s_2}{s_1-s_2}, & s_1 < s_i \le s_2 \\ \frac{\tau_t}{s_2-s_3}\cdot s_i - \frac{\tau_t\cdot s_3}{s_2-s_3}, & s_2 < s_i \le s_3 \end{cases} \tag{22}$$

$$G_{f,i} = \begin{cases} \frac{\tau_{max}\cdot s_i^2}{2\cdot s_1}, & 0 \le s_i \le s_1 \\ \frac{\tau_{max}\cdot s_1}{2} + [\tau_{max} - \frac{(\tau_{max}-\tau_t)\cdot(s_1-s_i)}{2(s_1-s_2)}]\cdot(s_i-s_1), & s_1 < s_i \le s_2 \\ \frac{\tau_{max}\cdot s_1+(\tau_{max}+\tau_t)(s_2-s_1)}{2} + [\tau_t - \frac{\tau_t\cdot(s_2-s_i)}{2(s_2-s_3)}]\cdot(s_i-s_2), & s_2 < s_i \le s_3 \end{cases} \tag{23}$$

$$G_{f,i} = f_4(s_i) \tag{24}$$

$$F_i = f_2(f_1^{-1}(f_4(s_i))) \tag{25}$$

where s_1, s_2, and s_3 are the slip at the maximum shear stress (τ_{max}), turning point with a shear stress of τ_t, and the maximum slip, respectively; τ_i, s_i, and $G_{f,i}$ are the shear stress, slip, and partial fracture energy, respectively, at position x_i along the bond line; F_i denotes the Fe-SMA internal tensile force at position x_i.

When simplifying the processed bond–slip behavior using the proposed bond–slip model, as written per Eq. (22), the partial fracture energy is expressed as Eq. (23). Substituting Eq. (23), which is denoted as Eq. (24), into Eq. (16) allows for simulation of the force–displacement ($F-\Delta$) behavior. Fig. 8 depicts a comparison between the experimentally measured load–displacement behavior (solid red, —) and the one simulated via Eq. (25) (dashed blue, – – –). A bond–slip behavior (solid red, —), which is processed on the basis of the experimentally measured load–displacement curve, is simplified to a triangular or trapezoidal curve (dashed blue, – – –). Input the simplified bond–slip (dashed blue, – – –) into the model (Eq. (25)) results in the computed load–displacement behavior (dashed blue, – – –). The excellent agreement between the experimental and computed load–displacement curve confirms the efficacy of the proposed nonlinear model in recovering the load–displacement behavior.

4. Numerical scheme for recovering the full-range mechanical behavior

4.1. Outline of the algorithm

Thus far, the focus has been on recovering the behavior at the loaded end of a joint (i.e., the bond–slip and force–displacement behaviors). This section proposes a numerical scheme based on the algorithm depicted in Fig. 9(a) to simulate the full-range behavior of the bonded joints, including the tensile strain, tensile stress, and shear stress in random positions along the bond line. The algorithm is described as follows:

1. Divide the adhesive bond into finite segments of length dx. The bond is assumed sufficiently long, to justify that all the stress, strain, and slip at the free end (left boundary in Fig. 2a) are zero.
2. Define an arbitrary strain increment dε (a suggested range is $10^{-4}-10^{-2}$).
3. Compute the strain predictor of the ith element by adding the strain increment dε to the strain of the (i-1)th element, $\varepsilon_i = \varepsilon_{i-1} + \mathrm{d}\varepsilon$.

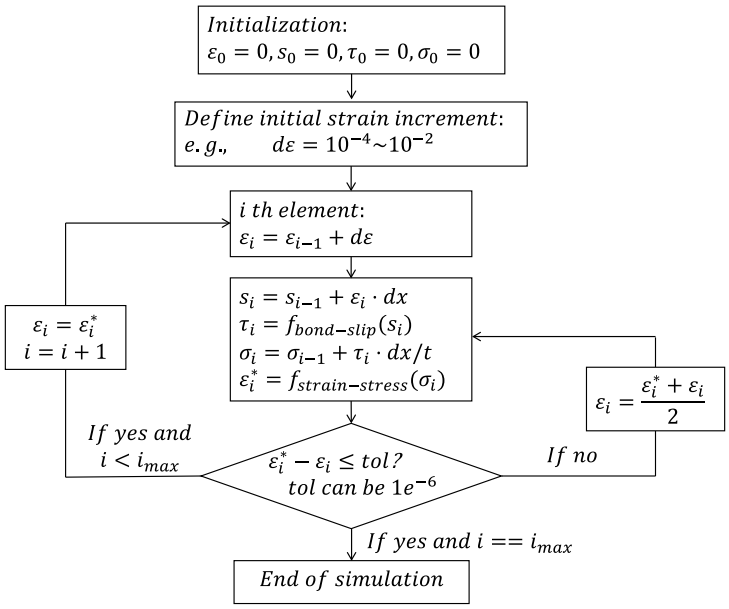

(a) Flowchart of the devised algorithm

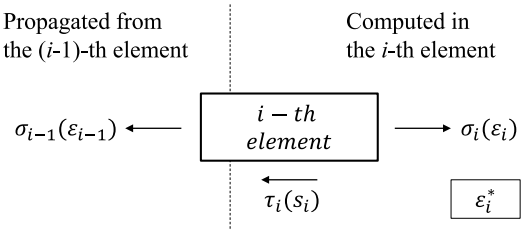

(b) Equilibrium of the i-th element

Fig. 9. The proposed numerical algorithm for computation of the full-range behavior of bonded joints.

4. Compute the behavior of the ith element (Fig. 9(b)):
   (a) The slip of the ith element is incrementally computed by adding the incremental deformation of the ith element, $s_i = s_{i-1} + \varepsilon_i \cdot \mathrm{d}x$.
   (b) The shear stress of the ith element is obtained by substituting the slip of the ith element into the bond–slip curve, $\tau_i = f_{bond-slip}(s_i)$ (Eq. (22)).
   (c) The tensile stress of the ith element is computed from equilibrium, $\sigma_i = \sigma_{i-1} + \tau_i \cdot \mathrm{d}x/t$, where t is the thickness of the Fe-SMA strip.
   (d) An updated strain (ε_i^*) of the ith element is computed via substituting the tensile stress of the ith element into the stress–strain curve, $\varepsilon_i^* = f_{strain-stress}(\sigma_i)$.
5. Check if the discrepancy between the strain predictor (ε_i) and the updated strain (ε_i^*) of the ith element lies within a specified tolerance. If yes, proceed to the next element. If not, define the strain predictor as the average of ε_i and ε_i^* and return to step 4.
6. The simulation is terminated when all elements are resolved.

4.2. Modification at the free end

The solution of the above algorithm in Section 4.1 is the behavior of a virtual joint with sufficiently long bond length, schematically illustrated as black curves in Fig. 10; the free end of this virtual joint is not loaded, and debonding occurs at the loaded end (adhesive bond fully damaged). In reality, however, the bond length is limited, and the damage will eventually propagate to the free end of the joint. Therefore, a modification, as schematically plotted in dashed red in Fig. 10, is adopted at the free end in

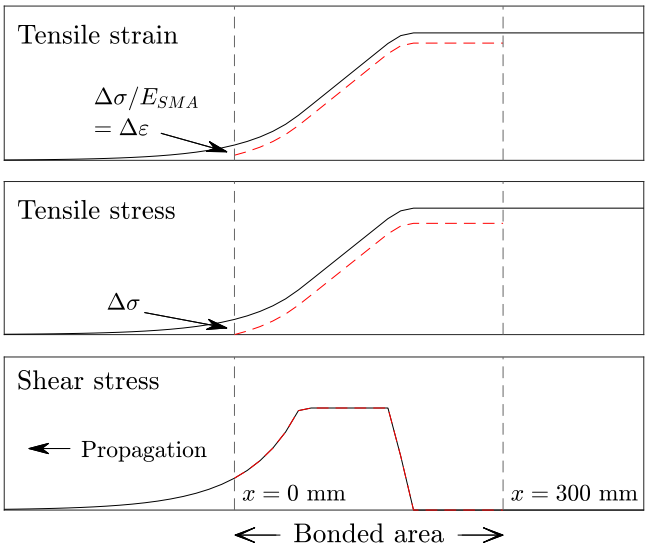

Fig. 10. Schematic modification of behaviors at the free end ($x = 0$ mm). The solid black curves reflect the result of the algorithm in Section 4.1, while the red dashed curves are results adopting modification (Eqs. (26) and (27)) at the free end.

order to simulate the debonding propagation there. The experimental studies delivered by Wang et al. [8] and Li et al. [9] revealed that when the tensile load reaches its maximum (i.e., the bond capacity), debonding initiates; afterwards, the tensile stress gradient, tensile strain gradient, and the shear stress profile do not change shape, but propagate toward the free end (this process is also known as debonding propagation). Therefore, in the model proposed herein, the stress and strain profiles shift through the bonded area (the area between the two black dashed lines in Fig. 10). When the front of the shear stress profile outreaches the free end, the shear force and the balancing tensile force decrease. Accordingly, the tensile stress and strain at the loaded end should reduce. In this case, the computed tensile stress and strain profiles move not only toward the free end but also downward. The tensile stress profile always crosses the point of $\sigma|_{x=0} = 0$ to justify the boundary condition of tensile stress being zero at the free end. This reduction of tensile stress is computed via Eq. (26). Correspondingly, the tensile strain profile should descend, and the value of strain reduction is estimated via elastic unloading, per Eq. (27). The tensile strain at the free end is supposed to be zero, since it lies on a free surface of the Fe-SMA strip. However, a residual strain (non-zero) at the free end would occur with adoption of the strain reduction via Eq. (27). The current model is unable to satisfy both the zero stress and zero strain conditions at the free end. This shortcoming could be addressed by means of more refined finite element modelling with proper material behavior as input, which though would result in higher computational effort. Since the stress behavior is of primary interest for engineering applications, we choose here to explicitly satisfy the zero stress condition at the free end.

$$\Delta\sigma = \frac{1}{t} \cdot \int_{-\infty}^{0} \tau \mathrm{d}x \tag{26}$$

$$\Delta\varepsilon = \frac{\Delta\sigma}{E_{SMA}} \tag{27}$$

where t denotes the thickness of Fe-SMA strip; E_{SMA} represent the elastic modulus of the Fe-SMA strip, which is 180 GPa according to Yang et al. [38].

During the propagation of these three profiles ($\varepsilon - x$, $\sigma - x$, and $\tau - x$) from the loaded end (right end) toward the free end (left end), the load–displacement ($F - \Delta$) behavior is computed as follows. The tensile force is computed as the multiplication of the tensile stress at the loaded end ($x = 300$ mm) and the cross-sectional area. The slip is estimated as the slip at the free end ($s(0)$), which is computed by substituting the partial fracture energy at the free end into inversed Eq. (24), plus the integral of the tensile strain from the free end ($x = 0$ mm) to the loaded end ($x = 300$ mm), i.e. $s = s(0) + \int_0^{300} \varepsilon \mathrm{d}x$.

The modelling results of the full-range behavior are depicted as dashed curves in Figs. 11 and 12, representing joints with a linear adhesive and joints with a nonlinear adhesive, respectively. The solid curves represent results that are derived from direct processing of the experimental measurements, i.e., without involvement of a numerical model. These processing steps will be introduced in Section 5. It should be noted that the proposed numerical model (ca. 2 s for each run on the computer of the first author) is approximately 100 times faster than an equivalent finite element simulation using the cohesive zone model in ABAQUS (ca. 5 min), with the same spatial resolution and similar accuracy for force and stress.

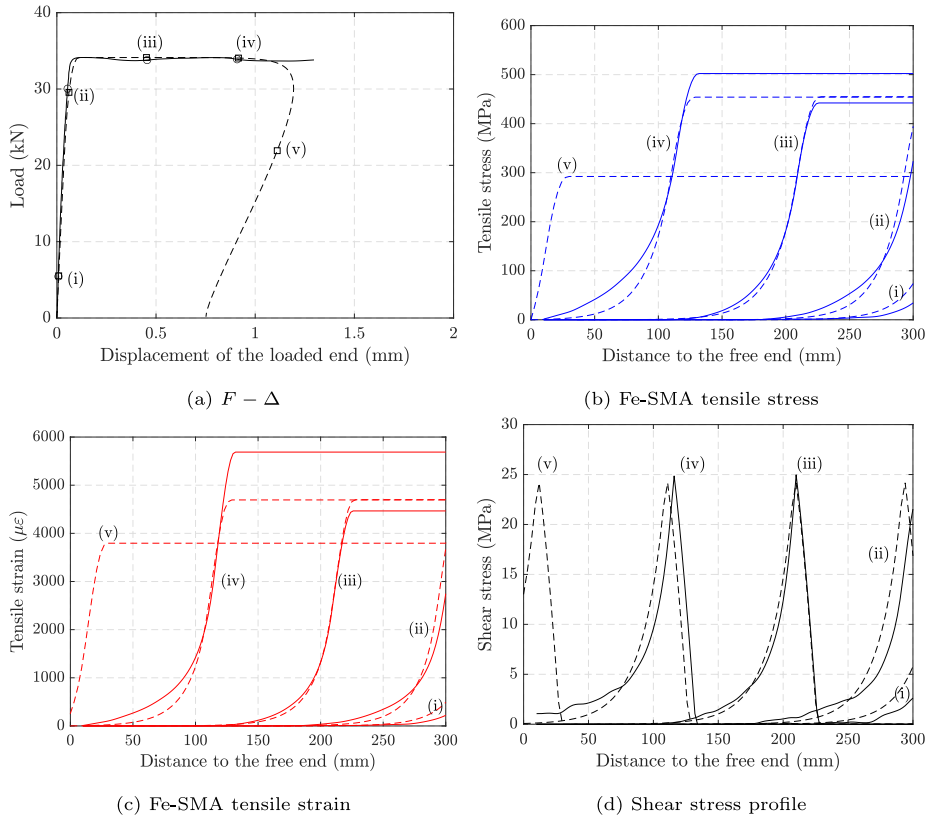

Fig. 11. Mechanical behaviors of joints with a linear adhesive. The solid curves represent the processed experimental behaviors, while the dashed curves are the modelling results.

4.3. Joint with linear adhesive

A simplified triangular bond–slip behavior is used as input to compute the mechanical behavior of a joint with a linear adhesive. The results are depicted as dashed curves in Fig. 11, which can be divided into four stages: (i) the elastic stage, (ii) the damage accumulation stage, (iii–iv) the debonding propagation stage, and (v) the descending stage (snap-back).

4.3.1. Elastic stage

At the beginning of loading, the tensile load remains at a low level (stage (i) in Fig. 11), and materials behave mostly in the elastic range. No damage occurs in the adhesive layer, and the Fe-SMA strip remains in the linear-elastic stage, as the maximum tensile stress (ca. 74 MPa) is below the limit of proportionality (ca. 120 MPa) [9].

4.3.2. Damage accumulation stage

As the load increases, the tensile stress and strain of the Fe-SMA strip increase, while the shear stress at the loaded end decreases after reaching a peak value of 24 MPa, indicating damage initiation and accumulation at the loaded end (stage (ii) in Fig. 11(d)). In this stage, the development of tensile stress and strain are no longer proportional, since the tensile stress (ca. 395 MPa) exceeds the limit of proportionality (ca. 120 MPa).

4.3.3. Debonding propagation stage

When the shear stress at the loaded end reduces to zero (stage (iii) in Fig. 11(d)), the adhesive bond at the loaded end is fully damaged, and the load–displacement behavior enters a plateau; debonding occurs and propagates gradually toward the free end (stages (iii) and (iv) in Fig. 11). In this stage, the displacement at the loaded end increases, while the tensile load remains constant; the tensile stress profile, the tensile strain profile, and the shear stress profile do not change shapes and values, but propagate toward the free end until the front of the shear stress profile reaches the free end (the free end is loaded).

At this stage, the maximum tensile stress and strain of the Fe-SMA strip are 450 MPa and 4700 $\mu\varepsilon$, respectively. Among the total tensile strain, the elastic strain contributes 2500 $\mu\varepsilon$, while the nonlinear strains (plastic strain and phase transformation strain) are 2200 $\mu\varepsilon$. This implies that the nonlinearity of Fe-SMA is not developed significantly, given that the elongation at break of Fe-SMA could reach 50% (500,000 $\mu\varepsilon$) [9]. Besides, it can be observed in Fig. 4 that the stress–strain behavior of the Fe-SMA remains

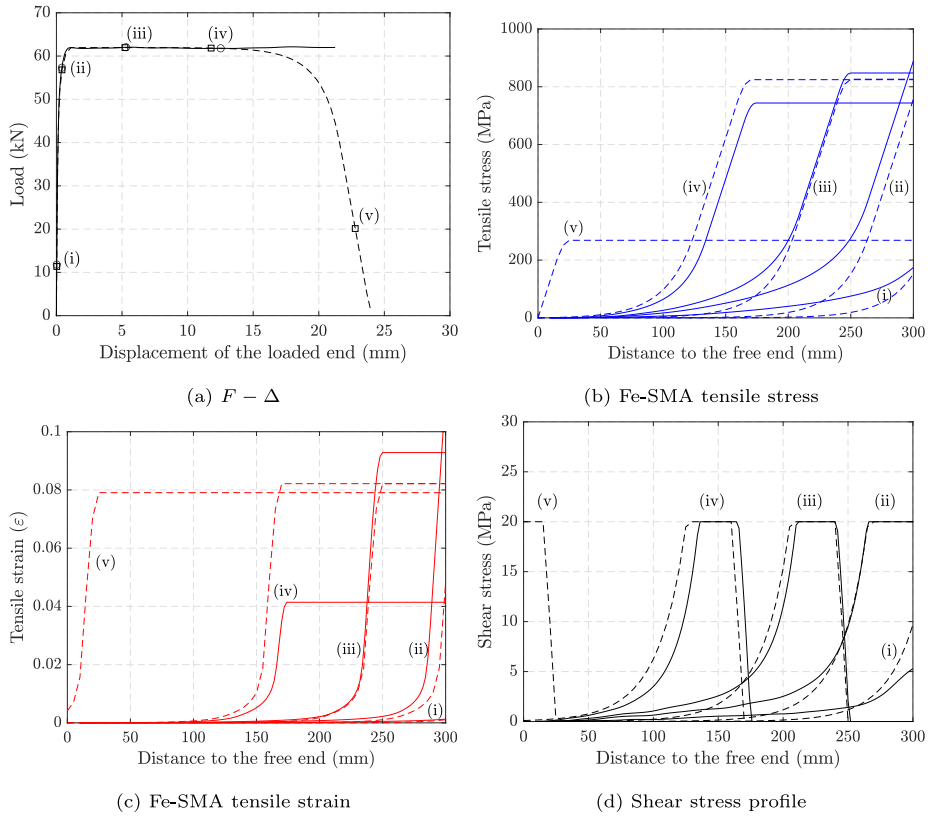

(a) $F - \Delta$ (b) Fe-SMA tensile stress

(c) Fe-SMA tensile strain (d) Shear stress profile

Fig. 12. Mechanical behaviors of joints with a nonlinear adhesive. The solid curves represent the processed experimental behaviors, while the dashed curves reflect the modelling results.

in a quasi-linear stage, if the tensile stress remains lower than 450 MPa. The observation of the undeveloped nonlinearity further supports the conclusion of an experimental study [9] that when a linear adhesive is used for bonding Fe-SMA to steel substrates, the Fe-SMA can be regarded as an elastic material, characterized by its secant modulus.

4.3.4. Descending stage (snap-back)

When the front of the shear stress profile exceeds the free end (stage (v) in Fig. 11(d)), the shear force and the balancing tensile load decrease, and the displacement at the loaded end decreases significantly after an initial slight increase (stage (v) in Fig. 11(a)). In the meantime, the tensile stress and strain of the Fe-SMA strip reduce. Note here that the load reduction, which is accompanied by a decrease in displacement, is not an unloading process. To the contrary, it is a further loading process after stage (iv), corresponding to a snap-back phenomenon. As the tensile load decreases, the elastic deformation of the Fe-SMA strip, which accounts for ca. 40% of the total deformation, recovers; this results in reduced displacement. Such a snap-back phenomenon has also been reported in the CFRP-to-steel and CFRP-to-concrete bonded joints [13,15,18,39,40]. It is worth noting that a full-range load–displacement ($F - \Delta$) behavior, which contains ascending, plateau, and descending stages (see Fig. 11(a)), is modelled by the proposed numerical scheme (Section 4.1) adopting a modification at the free end (see Fig. 10). On the other hand, the analytical model in Section 3.4 can only capture the ascending and plateau stages (see Fig. 8). The adopted assumption of a sufficiently long bond length in the analytical model does not allow for simulating a descending load–displacement behavior. Moreover, since during the modification of the behavior at the free end (see Fig. 10), the zero-stress condition is satisfied at this end, while the zero-strain condition is ignored, a strain error of up to 2200 $\mu\varepsilon$ is accumulated at the free end (see stage (v) in Fig. 11(c)).

4.4. Joint with nonlinear adhesive

A simplified trapezoidal bond–slip behavior is used as input to compute the mechanical behaviors of a joint with a nonlinear adhesive. The results are depicted as dashed curves in Fig. 12, and reveal a four stage behavior: (i) the elastic stage, (ii) the damage accumulation stage, (iii–iv) the debonding propagation stage, and (v) the descending stage (without snap-back).

4.4.1. Elastic stage

At the beginning of loading (stage (i) in Fig. 12), a joint with a nonlinear adhesive behaves similarly to a joint with a linear adhesive; the involved materials behave mostly elastically.

4.4.2. Damage accumulation stage

As the load and displacement increase, the Fe-SMA strip enters the nonlinear stage, and the shear stress profile exhibits a plateau (stage (ii) in Fig. 12(d)). This plateau is a result of the assumed simplified trapezoidal bond–slip behavior. In reality, such a plateau would be curved, rather than perfectly flat; evidence can be found in CFRP-to-steel lap-shear joints with nonlinear adhesives [11,41,42]. After the plateau, the shear stress decreases with increasing slip, which is a result of the accumulated damage in the adhesive layer.

4.4.3. Debonding propagation stage

When the shear stress at the loaded end reduces to zero, namely the adhesive at that point is fully damaged, the tensile load reaches its maximum (the bond capacity); debonding starts to propagate (stages (iii) and (iv) in Fig. 12). In this stage, the tensile load, tensile stress profile, strain profiles, and shear stress profile retain their shape and propagate toward the free end until the front of the shear stress profile reaches the free end of the joint.

At this stage, the maximum tensile stress and strain of the Fe-SMA strip lie at 825 MPa and 82,200 $\mu\varepsilon$ (0.082 ε), respectively. Among the total tensile strain, the elastic strain contributes 4400 $\mu\varepsilon$ (only ca. 5% of the total strain), while the nonlinear strains are 77,800 $\mu\varepsilon$ (ca. 95% of the total strain). This suggests that only minor deformation is attributed to the elastic deformation, and the nonlinearity of the Fe-SMA is fully developed.

4.4.4. Descending stage (without snap-back)

When the front of the shear stress profile moves beyond the free end, the shear force and balancing tensile load reduce, while the tensile stress and strain within the Fe-SMA strip decrease (stage (v) in Fig. 12). In this stage, the incremental deformation of the Fe-SMA strip comprises two parts. The first part pertains to a further loading of the Fe-SMA close to the free end; before this stage, the Fe-SMA close to the free end is merely loaded. The second refers to the elastic unloading of the already debonded region. As explained previously, in a joint with a nonlinear adhesive, the plastic deformation surpasses the elastic deformation. As a result, in the descending stage, where the load reduces, the displacement at the loaded end further increases, and the load–displacement behavior does not experience a snap-back (stage (v) in Fig. 12(a)). Again, due to the violation of the zero-strain condition at the free end (see Fig. 10), an error of $0-7.8\%$ strain is accumulated at this end (see stage (v) in Fig. 12(c)).

5. Experimental behavior and comparison with model results

A novel experimental data processing method, which is on the basis of the processed bond–slip ($\tau - s$) behavior in Section 3.3, is proposed in this section. The processed experimental results are then used to validate the numerical solution in Section 4.

5.1. Experimental data processing

During the lap-shear tests, the tensile force is measured by a load cell, while the full-field displacement is measured by the DIC technique. The full-field strain, which is processed by the DIC software on the basis of measured displacement, however, is not used in the current study. The experimental behavior is processed according to the following protocol, which we here introduce:

1. The slip ($s - x$) of the Fe-SMA strip, namely the relative displacement between the Fe-SMA strip and steel plate, is measured by the DIC technique.
2. The load–displacement ($F-\Delta$) behavior is obtained by synchronizing the force measured by the load cell and the displacement measured by DIC at the loaded end.
3. Processing the local bond–slip behavior ($\tau-s$) from the global load–displacement ($F-\Delta$) behavior, using the model introduced in Section 3.3.
4. Substituting the bond–slip ($\tau - s$) into $s - x$ to infer the shear stress behavior along the bond line ($\tau - x$), namely the shear stress profile.
5. Integration of the $\tau-x$ curve over x by adopting $\sigma|_{x=0} = 0$ yields the tensile stress profile ($\sigma-x$), expressed as $\sigma_i = \frac{1}{t}\cdot\int_0^{x_i}\tau \mathrm{d}x$, where σ_i and x_i represent the tensile stress and coordinate at point-i; t denotes the thickness of the Fe-SMA strip.
6. Further substituting the constitutive behavior ($\sigma - \varepsilon$) into $\sigma - x$ yields the tensile strain profile ($\varepsilon - x$).

It should be noted that the Fe-SMA is an elastoplastic material, whose unloading should follow its elastic modulus. However, in step 6, the constitutive behavior ($\sigma - \varepsilon$) is measured under a monotonic loading regime. As a result, in step 6, the loading and unloading of Fe-SMA follow the same path, which means that the Fe-SMA is treated as a nonlinear-elastic material during the whole process. Such a treatment facilitates the solution process, as the loading history of every point along the Fe-SMA strip can hardly be accessed during the test. However, a problem of inaccurate strain computation will be introduced due to the improper treatment of the nonlinear behavior of the Fe-SMA; this will be discussed in the next section.

5.2. The full-range behavior, experiment and modelling

The processed experimental behaviors (solid curves) along with a comparison against the modelling results (dashed curves) of two examples of joints with a linear adhesive and a nonlinear adhesive are demonstrated in Figs. 11 and 12, respectively.

5.2.1. Joint with linear adhesive

Fig. 11 depicts the full-range mechanical behavior of a joint with a linear adhesive. The processed experimental behaviors (solid curves) and the modelled behaviors (dashed curves), including the load–displacement curves, tensile stress profile, tensile strain profile, and shear stress profile, are reasonably similar in stages (i–iii), namely the elastic stage, the damage accumulation stage, and the beginning of debonding propagation stage. It should be noted that among all behaviors, only the experimental load–displacement ($F-\Delta$) behavior is directly measured during the test and may be considered as reliable, while the further results occur either via data-processing or via model-based computation. Since the modelled load–displacement ($F-\Delta$) behavior approximates the experimental measurement perfectly in stages (i–iv), it can be speculated that the modelling results are reliable to some extent.

In stage (iv), the end of debonding propagation stage, the free end starts to be loaded. The load–displacement ($F-\Delta$) behavior and shear stress profiles from the two methods (i.e., the numerical model and experimental data processing protocol) remain similar; however, the experimentally-derived tensile stress and corresponding tensile strain result higher than the simulation results. Since the experimentally measured tensile load does not further increase in this stage, it is unlikely that the tensile stress at the loaded end increases additionally after debonding. On the other hand, the good agreement between the simulated and measured load–displacement ($F-\Delta$) behavior in stage (iv) suggests that the modelling results are trustworthy. Further comparison between the shear stress from modelling and experimental processing indicates that the experimentally processed shear stress at the free end is slightly overestimated in stage (iv), resulting in overvalued tensile stress and strain.

Stage (v), the descending stage with snap-back of load–displacement ($F-\Delta$), cannot be captured by a loading regime with controlling displacement at the loaded end. As discussed in Section 4, such a snap-back phenomenon corresponds to a further loading regime at reduced force and displacement. Alternatively, a loading regime with controlling displacement at the free end might enable an experimental observation of such a snap-back phenomenon. The displacement (slip) at the free end increases monotonically during the loading process, and it can be employed as the control signal. The bond length should be short so that the free end is loaded in the beginning. Interested readers are referred to the work of Biolzi et al. [13] for a study of CFRP-to-concrete bonded joints for more details.

5.2.2. Joint with nonlinear adhesive

Fig. 12 depicts the full-range mechanical behavior of a joint with a nonlinear adhesive; the experimentally derived behaviors are depicted as solid curves, while the dashed curves are computed by the numerical model. The experimentally processed behavior and modelling results in stages (i–iii) are fairly well matched. As mentioned earlier, only the experimental load–displacement ($F-\Delta$) behavior is directly measured during the test and is reliable. The modelled load–displacement ($F-\Delta$) behavior approximates the experimental measurement perfectly in stages (i–iv), therefore, the modelling results should be trustworthy.

In stage (iv), at the end of the debonding propagation stage, the force displacement behavior and the shear stress profile from experimental processing and modelling well match. However, the processed tensile stress is slightly lower than that in the simulation, while the processed tensile strain is ca. 50% lower than that in the simulation. Since the measured tensile load does not decrease in stage (iv), the reduction of tensile stress is hard to believe being true. A comparison of the experimental shear stress against the simulated shear stress in stage (iv) suggests that the processed shear stress close to the loaded end is slightly undervalued. As a result, the accumulated tensile stress is underestimated. As mentioned in a previous section, the Fe-SMA is treated as a nonlinear-elastic material when processing the experimental behavior. A slight underestimation of tensile stress would result in huge drop of the tensile strain in the nonlinear branch of the Fe-SMA.

Stage (v), the descending stage, again cannot be captured during the test. Since the modelling suggests no snap-back, a even lower loading speed would enable a stable fracture process of the bond line with energy being dissipated by creating new surfaces of the adhesive bond and the elastic energy releasing of the Fe-SMA strip. As a result, the descending stage would appear, where a reduced load is accompanied by an increasing displacement.

The comparison between the experimental and modelling results indicates that the proposed data processing method and the numerical model are capable of capturing the observed mechanical behavior of the tested Fe-SMA-to-steel joints with a linear or a nonlinear adhesive in stages (i–iii) (i.e. the elastic stage, damage accumulation stage, and the beginning of the debonding propagation stage). At the end of the debonding propagation stage (stage (iv)), where the shear stress profile approaches the free end, the model sufficiently approximates the experimental results, namely the measured load–displacement behavior. However, the processed experimental shear stress is less accurate in stage (iv), resulting in accumulated error of the tensile stress, which is further propagated to the evaluated tensile strain. The error in the estimated tensile strain is amplified when the stress–strain enters the nonlinear branch. Nevertheless, stage (iv) is short before the final failure of a bonded joint, which is not allowed in engineering applications; actions of retrofitting and repair should be conducted earlier. Furthermore, the descending stage (stage (v)) might exist only in the laboratory with a fine control of loading signal and loading speed. Consequently, the proposed data processing method and the numerical model are deemed suitable to infer the mechanical behavior of adhesively bonded Fe-SMA-to-steel lap-shear joints.

6. Further validation on general classes of bonded joints in shear

The model proposed in this study not only suits the Fe-SMA-to-steel bonded joints, but also works for other types of bonded joints in shear. 24 additional bonded joints of general classes are collected from the literature; these are NiTi-SMA-to-CFRP pull-out joints [27], Fe-SMA-to-concrete pull-out joints [31], Fe-SMA-to-steel lap-shear joints [8] (not involved in Section 2), stainless steel-to-concrete pull-out joints [43], stainless steel-to-concrete lap-shear joints [43], CFRP-to-steel lap-shear joints [41], CFRP-to-concrete lap-shear joints [37,44], and CFRP-to-concrete pull-out joints [45]. Lap-shear joints are also known as pull-off joints.

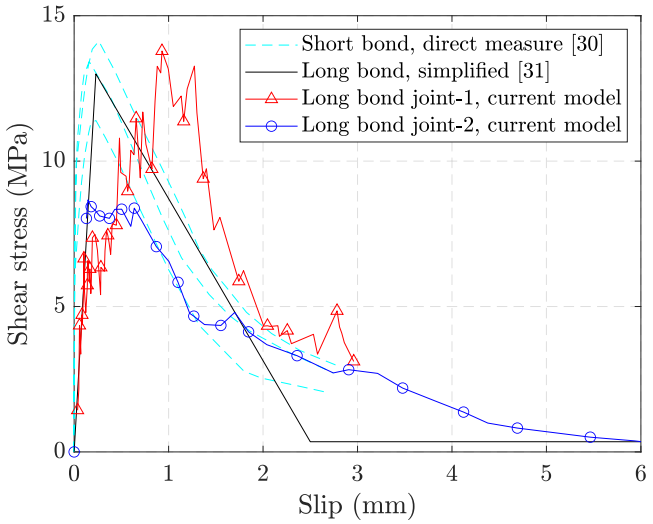

Fig. 13. Bond–slip behavior of pull-out joints of Fe-SMA rebars embedded in concrete blocks. The dashed light blue curves (– – –) are measured in pull-out specimens with short bond length [30]. The solid red curve with triangular marks (–Δ–) and the solid blue curve with circular marks (–○–) represent the bond–slip behavior of two pull-out joints with long bond length processed by the current model from load–displacement ($F-\Delta$) curves. The trilinear black curve (—) is a simplified bond–slip ($\tau-s$) behavior with the tail obtained from trial-and-error simulation to fit the experimentally measured load–displacement ($F-\Delta$) of joints with long bond length [31].

These bonded joints comprise (i) linear and nonlinear adherents, (ii) linear and nonlinear adhesives, (iii) lap-shear joints, where adherents are visible, and pull-out joints, where adherents are hidden, as well as (iv) several types of substrate materials, such as steel, concrete, and CFRP composites. The bond lengths of these joints are sufficiently long, meeting the long bond hypothesis. Since these bonded joints comprise various types of adherents, which can hardly be described by a universal $\sigma-\varepsilon$ model, Eqs. (11)–(13) are not suitable for all joints. Therefore, discretized $\sigma-\varepsilon$ is adopted, and the slop of adjacent points is used to represent the tangent modulus ($\mathrm{d}\sigma/\mathrm{d}\varepsilon$).

Fig. 13 illustrates several bond–slip curves of pull-out tests of Fe-SMA rebars embedded in concrete blocks [30,31]. The three dashed light blue curves (– – –) reflect the bond–slip behavior measured from three pull-out joints with the bond length being only 5 times of the rebar diameter [30]. The shear stress is an average shear stress, i.e., the tensile force in the rebar divided by the perimeter and the bond length, which is a typical method in inferring the bond behavior between concrete and steel rebar [46]. To properly model the experimental load–displacement behavior of the pull-out joints with long bond length (800 mm), a long tail determined by trial-and-error simulation was added in the bond–slip behavior after the three dashed blue curves [31], as shown in solid black (—). The solid red curves with triangular marks (–Δ–) and the solid blue curves with circular marks (–○–) are bond–slip behavior processed from the experimentally measured load–displacement behavior of pull-out joints with long bond length (800 mm) using the model in the current study as written in Eqs. (18)–(21). It is observed that the bond–slip curves processed from the model proposed in the current study, which assumes a long bond length, approximate fairly well the bond–slip curves processed from pull-out joints with short bond length, when the slip is less than 3 mm. The long tail in the blue bond–slip curve with circular marks (–○–), which cannot be measured in the case of a short bond, is able to be processed by the model in the current study; no trial-and-error simulation is needed.

The solid black bond–slip curve (—) in Fig. 13, which was simplified by Schranz et al. [31], is then inputted into the numerical model as described in Section 4 to compute the behavior of a pull-out joint, with the results illustrated as dashed blue curves (– – –) in Fig. 14. The solid black curves (—) are modelling results from Schranz et al. [31], where a classical second order differential equation (Eq. (28)) for CFRP bonded joints was employed by adopting the tangent modulus of Fe-SMA as a variable. Interested readers are referred to studies [15,17,18,31,44] for more details of employing Eq. (28). In the meantime, the red dots are the experimentally measured values.

$$\frac{\mathrm{d}^2 s}{\mathrm{d}x^2}-\tau\cdot\frac{4}{d_{SMA}\cdot E_{SMA}}=0 \tag{28}$$

where d_{SMA} and E_{SMA} are the diameter and tangent modulus of Fe-SMA rebar, respectively.

The current model and the Schranz model behave similarly when the tensile strain remains low and the shear stress is in the ascending branch (x = 0–560 mm) and the stage with residual shear stress (x = 650–800 mm). In the descending stage (x = 560–650 mm), the tensile strain from Schranz model increases faster while the shear stress drops faster compared with those from the current model. Since the Fe-SMA rebar is embedded in concrete block, DIC does not see the tensile strain within the scope of the bond line. Other techniques, such as strain gauges and fiber optics, are not able to measure a strain up to 10%. The only direct validation for the two models is the tensile strain measured by DIC at the loaded end; Schranz model and the current model

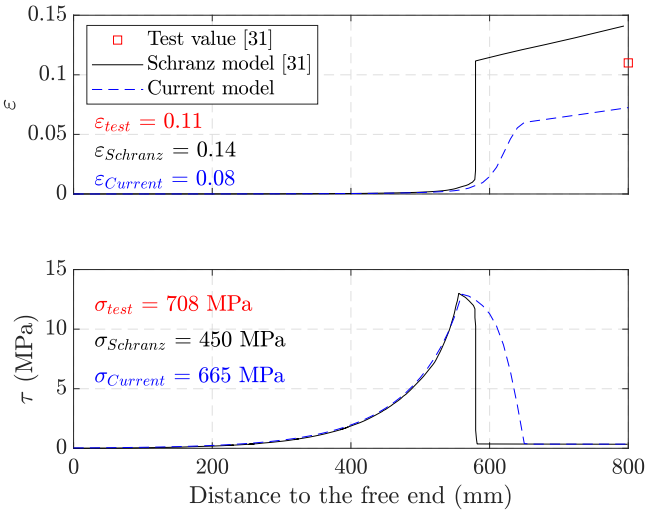

Fig. 14. Comparison between Schranz model (—) [31] and the current model (– – –), with experimental measurement (□) as support. The upper figure reflects the tensile strain of the Fe-SMA rebar, while the lower one represents the shear stress profile.

overestimates and underestimates an absolute strain of 3%, respectively. Another indirect experimental evidence is the tensile stress at the loaded end, which can be computed as the tensile force divided by the cross-sectional area. In the two models, the tensile stress is an integral of shear stress with respect to the coordinate, i.e., $\sigma_{end} = 4/d_{SMA} \cdot \int_0^{x_{end}} \tau \mathrm{d}x$. The Schranz model estimates a tensile stress of 450 MPa, while the current model estimates a tensile stress of 665 MPa, which is close to the experimental measurement of 708 MPa.

For the remaining of the 24 bonded joints collected from literature, their bond–slip ($\tau - s$) behavior is processed on the basis of the extracted load–displacement ($F - \Delta$) curves; the bond–slip ($\tau - s$) curves are simplified as a shape plotted in Fig. 7 and inputted in the numerical model, as illustrated in Fig. 9, to simulate their full-range mechanical behavior. Due to the constrained space of this paper, it is difficult to demonstrate the details as in Fig. 14 for all 24 bonded joints. Therefore, only the maximum tensile stress and strain of adherents are presented. Fig. 15 shows the comparison of stress and strain between the experimental measurement reported in the literature and the modelling results on the basis of the 26 Fe-SMA-to-steel lap-shear joints tested by the authors and the additional 24 joints extracted from the literature. The stress behavior is consistently simulated with high accuracy, while the strain simulation results less precise. When the strain level is low (less than 2%), the nonlinearity of the adherent is not fully developed; an accurate strain prediction and an accurate stress prediction are equivalent. When the strain level becomes high (larger than 5%), the stress–strain relationship of the adherents shifts to the nonlinear stage with a very small tangent modulus; the error in stress estimation is not as large as the one computed for strain. We conclude, on the basis of this broad applicability, that the numerical scheme proposed in this study is suited for simulation of the full-range mechanical behavior of various types of bonded joint subject to shear load.

7. Advantages and limitations of the proposed model and experimental data processing method

7.1. Advantages

A great advantage of the current model is, when computing the bond–slip ($\tau - s$) behavior from the load–displacement ($F - \Delta$) behavior, the current model does not rely on a dense or continuous measurement (e.g., dense strain gauges and full-field DIC) of the adherent behavior. The tensile load can be easily measured by a load cell; the displacement at the loaded end, though accessed by DIC in this study, can be measured by simple alternative techniques, such as Linear Variable Differential Transformer (LVDT) and Laser Displacement Transducer (LDT). With the bond–slip ($\tau - s$) behavior computed from the experimentally measured load–displacement ($F - \Delta$) behavior, the full-range mechanical behaviors are accessible via the numerical solution.

Another advantage of the current model is that for pull-out joints, whose bond–slip ($\tau - s$) has a stage with residual shear stress, the current model can directly compute the values of residual shear stress. No trail-and-error simulation, such as Schranz et al. [31] and El-Tahan and Dawood [27], is required.

Furthermore, the proposed numerical model is computationally efficient. It can be straightforwardly plugged into models of existing structures for strengthening/retrofitting analyses, without incurring additional computational burden, while it may further serve the purpose of parametric and stochastic analyses for studies related to reliability analyses and inverse problem settings (e.g. damage detection).

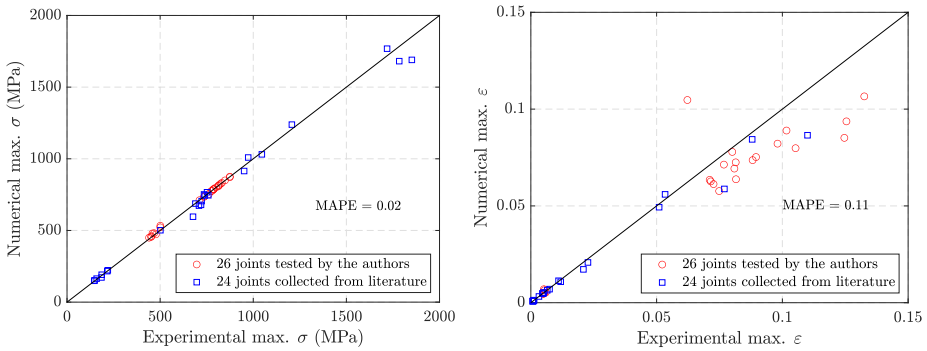

(a) Maximum tensile stress (b) Maximum tensile strain

Fig. 15. Comparison of adherent stress and strain between the modelling and experimental measurement.

Table A.1
Adhesive properties.

Material	E-modulus (MPa)	Tensile strength (MPa)	Elongation at break (%)
SikaPower 888	2100[a]	22[a]	3[a]

[a]Tested by the manufacturer [47].

Table A.2
Test matrix.

Specimen No.[a]	Specimen symbol	Fe-SMA type	Adhesive	Adhesive thickness (mm)	Bond capacity (kN)	Effective bond length (mm)	Failure mode[b]
25	NS-S3-T0.5–1	Non-prestrained	SikaPower 888	0.5	53.33	135	C
26	PS-S3-T0.5–1	Prestrained			59.09	140	C+R

[a]Specimens 1–24 were reported in Li et al. [9].
[b]C: cohesion failure; R: Fe-SMA strip rupture.

7.2. Limitations

As the available commercial Fe-SMA products are limited, it is uncertain whether the proposed two-term exponential stress–strain behavior, as written per Eq. (11), fits all Fe-SMAs, including those emerging in the future. An alternative is a numerical solution with the stress–strain behavior of the adherents being discretized, as described in Section 6. As a result, the model in Section 3 turns into a numerical rather than analytical model.

Despite the proven accuracy in computation of stress and force, the strain estimation of the current model for nonlinear adherents has room for improvement.

In the experimental data processing scheme, the Fe-SMA, which is an elastoplastic material, is treated as a nonlinear-elastic material, with loading and unloading following the same path. When the load and stress increase monotonically, this data processing scheme works quite well. However, with the presence of an unloading, slight stress error would introduce an unignorable error in strain (see stage (iv) of Fig. 12).

8. Conclusion

A semi-analytical and semi-numerical model is proposed in this study to simulate the mechanical behavior of Fe-SMA-to-steel adhesively bonded joints, with consideration of the nonlinear material response of both adherents and adhesives. The model delivers a means to bond capacity prediction, while further allows for simulation of the full-range mechanical behavior. A novel experimental data processing method is proposed for viewing the full-range mechanical behavior of bonded joints on the basis of the measured load–displacement ($F-\Delta$) behavior and slip of Fe-SMA strips. The following conclusions are drawn:

1. The proposed model succeeds in well-approximating the bond capacity when the interfacial fracture energy is known, and vice versa.
2. The model can be used to derive the local bond–slip ($\tau-s$) relationship from the experimentally measured global force–displacement ($F-\Delta$) behavior, without the need for supplementary strain measurements. This is different from the traditional processing method adopted in the state of the art.

3. A numerical scheme is proposed to simulate the full-range mechanical behavior of bonded joints. It is originally built and validated on the bases of 26 Fe-SMA-to-steel lap-shear joints. Its applicability for the simulation of general bonded joints in shear is further validated by 24 additional pull-out and lap-shear (pull-off) joints comprising different adherents (linear and nonlinear), adhesives (linear and nonlinear), and substrate materials.
4. An Fe-SMA-to-steel bonded joint with a linear adhesive behaves similarly to a CFRP bonded joint, since the nonlinearity of the Fe-SMA strip is not fully developed; a snap-back in the load–displacement ($F - \Delta$) behavior occurs. When the Fe-SMA strip is bonded with a nonlinear adhesive, evident nonlinear behavior of the Fe-SMA is developed, as its nonlinear strain contributes up to 95% of the total strain; the load–displacement ($F - \Delta$) experiences no snap-back, but reduction of force with increasing displacement.
5. The experimental behavior processed via a herein proposed data processing method is reliable until debonding approaching the free end. The snap-back in load–displacement ($F - \Delta$), which occurs with a linear adhesive, cannot be captured via a control of displacement at the loaded end.

CRediT authorship contribution statement

Lingzhen Li: Writing – original draft, Methodology, Investigation, Formal analysis, Conceptualization. **Eleni Chatzi:** Writing – review & editing, Supervision, Formal analysis. **Elyas Ghafoori:** Writing – review & editing, Supervision, Formal analysis, Conceptualization.

Declaration of competing interest

The authors declare that they have no known competing financial interests or personal relationships that could have appeared to influence the work reported in this paper.

Data availability

The Matlab code used for the analysis will be available in Github upon the acceptance of the manuscript.

Acknowledgments

The first author would like to acknowledge the financial co-sponsorship of the China Scholarship Council (CSC) for this PhD study. Sika AG and Huntsman GmbH are acknowledged for providing adhesives. The authors wish to express their gratitude to re-fer AG, Switzerland, for providing the Fe-SMA materials.

Appendix A. Two new lap-shear tests

Two Fe-SMA-to-steel lap-shear specimens, one with a non-prestrained Fe-SMA strip and the other with a prestrained Fe-SMA strip, were tested recently by the authors. A nonlinear adhesive, SikaPower 888 with the properties listed in Table A.1, provided by Sika AG (Switzerland), was employed to bond the Fe-SMA strips to the steel substrates. Apart from the adhesive, the rest are identical to those in the experimental study delivered by the authors [9], which contain: (i) the geometry of specimens, (ii) the types of Fe-SMA strips and steel plates, (iii) the specimen preparation, including the DIC pattern, (iv) the testing procedure, and (v) the post-processing procedure. The test results are listed in Table A.2.

Appendix B. Code

The Matlab code used for the analysis is available in Github (https://github.com/Lingzhen-Li/Fe-SMA-to-steel_debonding_model).

References

[1] Izadi M, Hosseini A, Michels J, Motavalli M, Ghafoori E. Thermally activated iron-based shape memory alloy for strengthening metallic girders. Thin-Walled Struct 2019;141:389–401.
[2] Vůjtěch J, Ryjáček P, Matos JC, Ghafoori E. Iron-based shape memory alloy for strengthening of 113-year bridge. Eng Struct 2021;248:113231.
[3] Fritsch E, Izadi M, Ghafoori E. Development of nail-anchor strengthening system with iron-based shape memory alloy (Fe-SMA) strips. Constr Build Mater 2019;229:117042.
[4] Wang W, Li L, Hosseini A, Ghafoori E. Novel fatigue strengthening solution for metallic structures using adhesively bonded Fe-SMA strips: A proof of concept study. Int J Fatigue 2021;148:106237.
[5] Hosseini E, Ghafoori E, Leinenbach C, Motavalli M, Holdsworth SR. Stress recovery and cyclic behaviour of an Fe–Mn–Si shape memory alloy after multiple thermal activation. Smart Mater Struct 2018;27(2):025009.
[6] Izadi M, Ghafoori E, Motavalli M, Maalek S. Iron-based shape memory alloy for the fatigue strengthening of cracked steel plates: Effects of re-activations and loading frequencies. Eng Struct 2018;176:953–67.
[7] Cladera A, Weber B, Leinenbach C, Czaderski C, Shahverdi M, Motavalli M. Iron-based shape memory alloys for civil engineering structures: An overview. Constr Build Mater 2014;63:281–93.
[8] Wang W, Hosseini A, Ghafoori E. Experimental study on Fe-SMA-to-steel adhesively bonded interfaces using DIC. Eng Fract Mech 2021;244:107553.

[9] Li L, Wang W, Chatzi E, Ghafoori E. Experimental investigation on debonding behavior of Fe-SMA-to-steel joints. Constr Build Mater 2023;364:129857.
[10] Li L, Chen T, Liu R. Rapid SIF calculation of inclined cracked steel plates bonded with CFRP materials, prestressed and non-prestressed. In: International conference on fibre-reinforced polymer (FRP) composites in civil engineering. Springer; 2021, p. 2247–57.
[11] Yu T, Fernando D, Teng J, Zhao XL. Experimental study on CFRP-to-steel bonded interfaces. Composites B 2012;43(5):2279–89.
[12] Fawzia S, Al-Mahaidi R, Zhao X-L. Experimental and finite element analysis of a double strap joint between steel plates and normal modulus CFRP. Compos Struct 2006;75(1–4):156–62.
[13] Biolzi L, Ghittoni C, Fedele R, Rosati G. Experimental and theoretical issues in FRP-concrete bonding. Constr Build Mater 2013;41:182–90.
[14] Martinelli E, Hosseini A, Ghafoori E, Motavalli M. Behavior of prestressed CFRP plates bonded to steel substrate: Numerical modeling and experimental validation. Compos Struct 2019;207:974–84.
[15] Fernando D, Yu T, Teng J-G. Behavior of CFRP laminates bonded to a steel substrate using a ductile adhesive. J Compos Constr 2014;18(2):04013040.
[16] Dai J, Ueda T, Sato Y. Development of the nonlinear bond stress-slip model of fiber reinforced plastics sheet-concrete interfaces with a simple method. J Compos Constr 2005;9(1):52–62.
[17] Wu Z, Yuan H, Niu H. Stress transfer and fracture propagation in different kinds of adhesive joints. J Eng Mech 2002;128(5):562–73.
[18] Yuan H, Teng J, Seracino R, Wu Z, Yao J. Full-range behavior of FRP-to-concrete bonded joints. Eng Struct 2004;26(5):553–65.
[19] Xia S, Teng J. Behaviour of FRP-to-steel bonded joints. In: Proceedings of the international symposium on bond behaviour of FRP in structures. International Institute for FRP in Construction; 2005, p. 419–26.
[20] Wang H-T, Wu G. Bond-slip models for CFRP plates externally bonded to steel substrates. Compos Struct 2018;184:1204–14.
[21] Gao W, Teng J, Dai J-G, et al. Effect of temperature variation on the full-range behavior of FRP-to-concrete bonded joints. J Compos Constr 2012;16(6):671–83.
[22] Silvestru V-A, Deng Z, Michels J, Li L, Ghafoori E, Taras A. Application of an iron-based shape memory alloy for post-tensioning glass elements. Glass Struct Eng 2022;1–24.
[23] Deng Z, Silvestru V-A, Michels J, Li L, Ghafoori E, Taras A. Performance of glass to iron-based shape memory alloy adhesive shear joints with different geometry. In: Challenging glass conference proceedings. 8, 2022.
[24] Muntasir Billah A, Alam MS. Bond behavior of smooth and sand-coated shape memory alloy (SMA) rebar in concrete. Structures 2016;5:186–95.
[25] Islam K, Billah AM, Chowdhury MMI, Ahmed KS. Exploratory study on bond behavior of plain and sand coated stainless steel rebars in concrete. Structures 2020;27:2365–78.
[26] Daghash SM, Ozbulut OE. Bond–slip behavior of superelastic shape memory alloys for near-surface-mounted strengthening applications. Smart Mater Struct 2017;26(3):035020.
[27] El-Tahan M, Dawood M. Bond behavior of NiTiNb SMA wires embedded in CFRP composites. Polym Compos 2018;39(10):3780–91.
[28] Dawood M, El-Tahan M, Zheng B. Bond behavior of superelastic shape memory alloys to carbon fiber reinforced polymer composites. Composites B 2015;77:238–47.
[29] Yuan G, Bai Y, Jia Z, Hui D, Lau K-t. Enhancement of interfacial bonding strength of SMA smart composites by using mechanical indented method. Composites B 2016;106:99–106.
[30] Schranz B, Czaderski C, Vogel T, Shahverdi M. Bond behaviour of ribbed near-surface-mounted iron-based shape memory alloy bars with short bond lengths. Mater Des 2020;191:108647.
[31] Schranz B, Czaderski C, Vogel T, Shahverdi M. Bond investigations of prestressed, near-surface-mounted, ribbed memory-steel bars with full bond length. Mater Des 2020;196:109145.
[32] Schranz B, Nunes MF, Czaderski C, Shahverdi M. Fibre optic strain measurements for bond modelling of prestressed near-surface-mounted iron-based shape memory alloy bars. Constr Build Mater 2021;288:123102.
[33] He J, Xian G. Bond-slip behavior of fiber reinforced polymer strips-steel interface. Constr Build Mater 2017;155:250–8.
[34] Wu C, Zhao X, Duan WH, Al-Mahaidi R. Bond characteristics between ultra high modulus CFRP laminates and steel. Thin-Walled Struct 2012;51:147–57.
[35] Zhou H, Fernando D, Torero JL, Torres JP, Maluk C, Emberley R. Bond behavior of CFRP-to-steel bonded joints at mild temperatures: experimental study. J Compos Constr 2020;24(6).
[36] Doroudi Y, Fernando D, Hosseini A, Ghafoori E. Behavior of cracked steel plates strengthened with adhesively bonded CFRP laminates under fatigue loading: Experimental and analytical study. Compos Struct 2021;266:113816.
[37] Zhu H, Wu G, Shi J, Liu C, He X. Digital image correlation measurement of the bond–slip relationship between fiber-reinforced polymer sheets and concrete substrate. J Reinf Plast Compos 2014;33(17):1590–603.
[38] Yang Y, Breveglieri M, Shahverdi M. Effect of phase changes on the axial modulus of an FeMnSi-shape memory alloy. Materials 2021;14(17).
[39] Martinelli E. Closed-form solution procedure for simulating debonding in FRP strips glued to a generic substrate material. Fibers 2021;9(4):22.
[40] Yang Y, Biscaia H, Chastre C, Silva MA. Bond characteristics of CFRP-to-steel joints. J Construct Steel Res 2017;138:401–19.
[41] Li L, Pichler N, Chatzi E, Ghafoori E. Estimation of the mechanical behavior of CFRP-to-steel bonded joints with quantification of uncertainty. Eng Struct 2022;266:114573.
[42] Wang H-T, Wu G, Dai Y-T, He X-Y. Experimental study on bond behavior between CFRP plates and steel substrates using digital image correlation. J Compos Constr 2016;20(6):04016054.
[43] Biscaia H, Franco N, Chastre C. Stainless steel bonded to concrete: an experimental assessment using the DIC technique. Int J Concr Struct Mater 2018;12(1):1–20.
[44] Czaderski C, Soudki K, Motavalli M. Front and side view image correlation measurements on FRP to concrete pull-off bond tests. J Compos Constr 2010;14(4):451.
[45] Seo S-Y, Feo L, Hui D. Bond strength of near surface-mounted FRP plate for retrofit of concrete structures. Compos Struct 2013;95:719–27.
[46] ASTM. Standard test method for comparing concretes on the basis of the bond developed with reinforcing steel. ASTM international west conshohocken, ASTM; 1991.
[47] Sika A. Product data sheet SikaPower-888. 2023, https://industry.sika.com/en/home/transportation/specialty-vehicles/sikapower-880.html, Last accessed on 2023-01-10.